

Automatic Differentiation for Second Renormalization of Tensor Networks

Bin-Bin Chen,^{1,2} Yuan Gao,¹ Yi-Bin Guo,^{3,4} Yuzhi Liu,⁵ Hui-Hai Zhao,⁶
 Hai-Jun Liao,^{3,4} Lei Wang,^{3,7} Tao Xiang,^{3,4,8} Wei Li,^{1,*} and Z. Y. Xie^{9,†}

¹*School of Physics, Key Laboratory of Micro-Nano Measurement-Manipulation and Physics (Ministry of Education), Beihang University, Beijing 100191, China*

²*Physics Department, Arnold Sommerfeld Center for Theoretical Physics, and Center for NanoScience, Ludwig-Maximilians-Universität, Theresienstrasse 37, 80333 Munich, Germany*

³*Institute of Physics, Chinese Academy of Sciences, P.O. Box 603, Beijing 100190, China*

⁴*School of Physics, University of Chinese Academy of Sciences, Beijing 100049, China*

⁵*Department of Physics, Indiana University, Bloomington, Indiana 47405, USA*

⁶*Alibaba Quantum Laboratory, Alibaba Group, Beijing, China*

⁷*Songshan Lake Materials Laboratory, Dongguan, Guangdong 523808, China*

⁸*Kavli Institute for Theoretical Sciences, University of Chinese Academy of Sciences, Beijing 100190, China*

⁹*Department of Physics, Renmin University of China, Beijing 100872, China*

(Dated: December 6, 2019)

Tensor renormalization group (TRG) constitutes an important methodology for accurate simulations of strongly correlated lattice models. Facilitated by the automatic differentiation technique widely used in deep learning, we propose a uniform framework of differentiable TRG (∂ TRG) that can be applied to improve various TRG methods, in an automatic fashion. Essentially, ∂ TRG systematically extends the concept of second renormalization [PRL 103, 160601 (2009)] where the tensor environment is computed recursively in the backward iteration, in the sense that given the forward process of TRG, ∂ TRG automatically finds the gradient through backpropagation, with which one can deeply “train” the tensor networks. We benchmark ∂ TRG in solving the square-lattice Ising model, and demonstrate its power by simulating one- and two-dimensional quantum systems at finite temperature. The deep optimization as well as GPU acceleration renders ∂ TRG manybody simulations with high efficiency and accuracy.

Introduction.— In the investigation of strongly correlated quantum states and materials, tensor renormalization group (TRG) constitutes a thriving field and are playing an increasingly important role recently [1–4]. TRG is a diverse family of approaches, including the coarse-graining TRG [5, 6], higher-order TRG (HOTRG) [7], tensor network renormalization [8–11], etc. They have been put forward to evaluate classical statistical systems as well as expectation values out of two-dimensional (2D) tensor network states [12]. There are also TRG methods developed to simulate d -dimensional quantum lattice models at finite temperature T [13–20], whose Euclidean path integral constitutes a $(d + 1)$ -dimensional worldsheet.

In the course of TRG process, environment of local tensors should be considered for conducting a precise truncation through isometric renormalization transformations in tensor bases. This can be traced back to the renowned density matrix renormalization group algorithm [21], where the effects of environment are reflected in the reduced density matrix. For generic tensor networks, second renormalization group (SRG) has been proposed to improve the tensor renormalization [7, 22–24]. In SRG, the environment of local tensors is computed recursively between different scales of a hierarchical network, with which a global optimization is feasible.

Recently, profound interplay between deep learning and tensor network algorithms has raised great interest [25–33]. Among others, the differentiable programming is of partic-

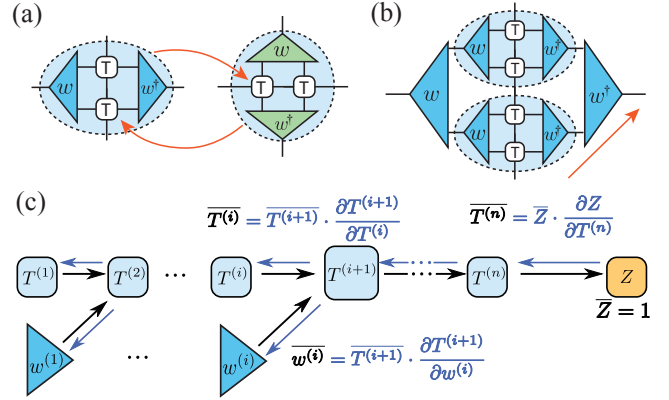


FIG. 1. (Color online) (a) shows a TRG step where the scale transformations w are introduced along both directions, while only vertical renormalization is involved in (b), which eventually compresses the tensor network into a 1D structure that can then be contracted exactly. (c) plots the computational graph of the forward TRG process as well as the backpropagation.

ular interest for tensor networks. Given the computational graph generated in forward process, the gradient of corresponding variables can be calculated through the chain rule of derivatives in the backpropagation, with which the neural network can be deeply trained. The automatic calculation of gradients can be obtained within machine precision, and with same computational complexity of forward process. Very recently, this idea of differentiable programming that exploits automatic differentiation and gradient based optimization, has been introduced to optimize tensor networks [34].

* w.li@buaa.edu.cn

† qingtaoxie@ruc.edu.cn

In this work, we regard the renormalization transformation as input parameters of the TRG program, and point out that the SRG backward iteration bears a correspondence with the backpropagation algorithm in differentiable programming. Inspired by this substantial connection, we turn the idea of SRG into a generalized versatile framework, differentiable TRG (∂ TRG). In ∂ TRG, the forward TRG process is made fully differentiable, and the renormalization transformations are optimized globally and automatically through the backpropagation. We apply ∂ TRG to simulate thermal equilibrium states at finite temperature, and achieve significantly improved accuracy over previous methods [13, 19]. The efficiency is demonstrated by implementing ∂ TRG with PyTorch [35, 52], which facilitates the GPU computing and shows a high performance of about 40 times acceleration over a single CPU core.

Correspondence between SRG and backpropagation.— Backpropagation is a widely used method for training deep neural networks [36–38], where the gradients of parameters can be computed through a reverse-mode automatic differentiation (see SM. C). On the other hand, SRG plays a very similar role in tensor algorithms as backpropagation. To be specific, as shown in Figs. 1(a,c), a hierarchical tensor network can be constructed by piling up a series of isometric RG transformations $\{w^{(i)}\}$, with $i = 1, 2, \dots, n$ for each layer. In a well-designed TRG program, the input tensor $\{w^{(i)}\}$ are successively applied to the tensors T and the output can be a tensor trace in general, e.g., partition function of a statistical system.

SRG takes the job to further optimize the renormalization transformations $\{w^{(i)}\}$ in the backward iteration, by making use of the environment. An adjoint tensor of $w^{(i)}$ at scale i is defined as the gradient $\overline{w^{(i)}} \equiv \frac{\partial Z}{\partial w^{(i)}}$, which can be related to the environment through

$$E_w^{(i)} = \frac{1}{N_i} \overline{w^{(i)}}, \quad (1)$$

where N_i denotes the times $w^{(i)}$ appearing in the network, and Z the tensor trace to be maximized. It directly follows from Eq. (1) that the recursive relations used in the backward iteration to determine $\{E^{(i)}\}$ in SRG, can be recasted into the derivative chain rule form, as depicted in Fig. 1(c). Remind that the multiplications there with Jacobians $\partial T^{(i+1)}/\partial T^{(i)}$ and $\partial T^{(i+1)}/\partial w^{(i)}$, etc, are conducted implicitly. They constitute sequences of tensor contractions exactly equivalent to the recursive tensor contractions in SRG (c.f. SM. B and SM. E).

Differentiable tensor renormalization group. — Being aware of the intimate relation between the backpropagation and SRG, we now extend the latter to a more flexible framework, ∂ TRG, with the help of well-developed automatic differentiation packages [39], e.g., autograd [51] and PyTorch [35, 52]. With these facilities, ∂ TRG can record all operations performed on the input variables (tensors), and compute the derivatives [e.g. Eq. (1)] automatically in the backward iterations. Given the gradients, we can find the optimal parameters $\{w^{(i)}\}$ for the TRG forward process. Not limited within the original proposals [7, 22], the idea of SRG can be applied

to various TRG schemes through this differentiable programming. Below, we consider two different ∂ TRG schemes following the HOTRG [7] and exponential TRG (XTRG) [19], as shown in Figs. 1(a) and (b), respectively.

Once the environment $E_w^{(i)}$ is obtained, one can resort to, e.g., standard quasi-Newton optimization method (SM. D), or quasi-optimal schemes through tensor decompositions of $E_w^{(i)}$ [7, 22], for the optimization of $w^{(i)}$. Remind that a tensor decomposition scheme that keeps $w^{(i)}$ isometric has been developed in the context of multi-scale entanglement renormalization ansatz (MERA) algorithm [40, 41], which are mainly adopted in the simulations below. MERA update performs a singular value decomposition (SVD) $E_w = USV^\dagger$ and updates $w = UV^\dagger$, which maximizes the cost function $Z = \text{Tr}(E_w \cdot w)$, with $O(D^4)$ time complexity. Here D is the bond dimension as introduced in SM. D.

Due to the intrinsic nonlinearity (in w) in the optimization problem, n_i inner iterations (in practice $n_i = 5-10$) are introduced in a single step of MERA update. Moreover, thanks to the convenient access to $E_w^{(i)}$, in ∂ TRG we can deeply optimize the tensor network via sweep optimizations. In practice, we scan from inner to outer layers n_s times until the results converge, thus assure a highly accurate global update of $\{w^{(i)}\}$ tensors.

∂ TRG of 2D Ising model.— As a first demonstration, we apply ∂ TRG, with two specific implementations in Fig. 1(a,b), to solve the classical Ising model on the square lattice. Following the standard procedure, we can write down a square-lattice tensor network representation consisted of rank-4 tensors T , whose contraction through TRG results in the partition function Z (see SM. A for details).

In Fig. 1(a), after n steps of renormalizations, we obtain a single tensor representing the whole system of $2^n \times 2^n$ sites (in

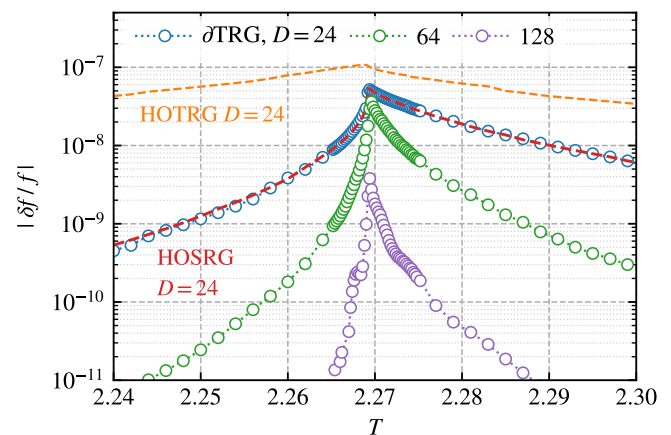


FIG. 2. (Color online) The relative errors of free energy $|\delta f/f|$ in the vicinity of critical temperature T_c , obtained from HOTRG, HOSRG, and ∂ TRG methods. We perform $n_i = 5-10$ iterations within each MERA update, and the total number of sweeps n_s ranges from a few iterations to a few hundreds, depending on the specific temperature and scheme, until the relative errors reach a convergence criterion of $\epsilon = 10^{-4}$. The $D = 24$ ∂ TRG calculations follows the scheme in Fig. 1(a), while $D = 64$ and 128 curves the scheme in Fig. 1(b).

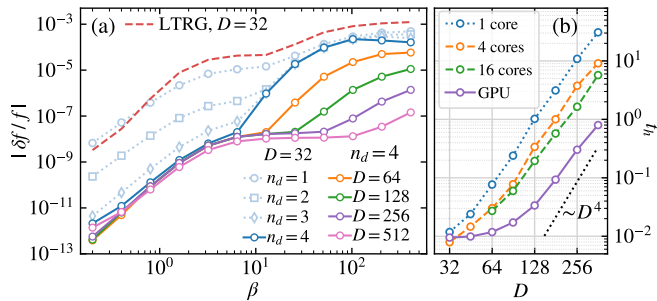


FIG. 3. (Color online) (a) Comparisons of relative errors of free energy between linearized TRG (LTRG) and ∂ TRG. In the initial $\rho(\tau)$ of ∂ TRG, $\tau \approx 5 \times 10^{-5}$, which is also used as the Trotter slice in the LTRG calculations. The results are shown with optimization depth $n_d \leq 4$, $n_i = 10$ in a single MERA update, and overall sweep iterations $n_s = 3$. (b) Comparisons of the computational walltime of ∂ TRG on GPU and CPU with up to 16 cores, benchmarked on the infinite XY chain. The calculations are carried out on Nvidia Tesla V100 GPU and Intel Xeon 6230 CPU, with retained bond dimensions up to $D = 360$. The dashed line depicts the scaling $t_h \sim D^4$.

practice $n = 25$ guarantees the thermodynamic limit), whose self-contraction leads to the partition function Z . On the other hand, after n steps of renormalization, one arrives at an effective 1D system, whose complete contraction also leads to an accurate measure of the partition function.

In Fig. 2, we show the accuracies of ∂ TRG implementations, together with the HOTRG and HOSRG data for comparisons. Owing to the sweep update, ∂ TRG leads to errors clearly smaller than those of HOTRG, while achieving, as expected, the same accuracies as HOSRG [50].

The two schemes of ∂ TRG in Figs. 1(a) and (b) have different computational costs. The latter is considerably less resource-demanding, i.e., $O(D^4)$ in computational time, while it is $O(D^7)$ in Fig. 1(a). The memory costs are also dramatically different, i.e., $O(D^5)$ for Fig. 1(a) and $O(D^3)$ for (b). Therefore, we can push the ∂ TRG simulations in Fig. 1(b) with bond states up to $D = 128$, reaching much higher precision as shown in Fig. 2. From the comparison shown in Fig. 2, as well as other considerations, we chose the ∂ TRG scheme in Fig. 1(b) to simulate quantum models as presented below.

Infinite quantum XY chain.— Now we employ ∂ TRG to simulate the exactly solvable quantum XY chain

$$H_{XY} = \sum_{(i,j)} S_i^x S_j^x + S_i^y S_j^y. \quad (2)$$

We start with preparing the density matrix $\rho(\tau)$ through (second order) Trotter-Suzuki decomposition (see SM.F). A very small imaginary-time step τ is chosen to ensure that Trotter errors are negligible. Given the matrix product operator (MPO) representation of $\rho(\tau)$, we proceed to cool down the system exponentially fast, with the ∂ TRG algorithm shown in Fig. 1(b). The results are shown in Fig. 3(a), where the relative error $|\delta f/f|$ curves rise up from very small values at high temperature and increase monotonically as T decreases.

In Fig. 3(a), we compare the relative errors $|\delta f/f|$ between ∂ TRG and LTRG, where the latter follows a cooling proce-

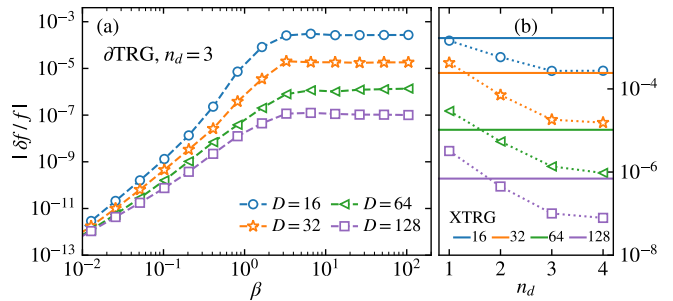


FIG. 4. (Color online) (a) Relative errors of transverse-field Ising model on a 4×4 open square lattice, at critical transverse field $h = h_c$. (b) ∂ TRG results with various D are plotted versus optimization depths $n_d = 1, 2, 3$ and 4. The comparison is at a fixed low temperature $\beta \approx 105$, and the standard XTRG results are shown with solid lines.

dure linear in β ($\equiv 1/T$) [13]. It is observed that ∂ TRG with depth $n_d = 1$ (i.e., optimizing exclusively the current layer in the course of cooling) already outperforms LTRG in both efficiency and accuracy. By sweeping into n_d (up to 4) layers, the accuracy is found to improve continuously in the relatively high to intermediate temperature regime due to better optimization. At low temperature, on the other hand, the enhancement of accuracy is marginal due to the limited expressibility of the tensor network with a given bond dimension $D = 32$. Therefore, we show also in Fig. 3(a) the results of larger bond dimensions (up to 512), with a fixed depth $n_d = 4$. There we observe that $|\delta f/f|$ decreases monotonically and attains very high accuracy, with relative error $\sim 10^{-7}$ at low temperature (down to $\beta \approx 400$).

GPU acceleration.— We implement ∂ TRG with the open source library PyTorch, and take advantage of GPU computing to significantly accelerate the simulations. In Fig. 3(b), we show the elapsed hours t_h versus D in the simulations of infinite XY chain on GPU and CPU, respectively. To quantify the speedup, t_h is monitored at $\beta = 12.8$, where the computation time falls well into a logarithmic scaling regime vs. β , i.e., $t_h \propto \ln \beta$ (see SM.G).

From Fig. 3(b), we observe approximately 40 times GPU acceleration (for $D = 360$ calculations), as compared to single core CPU calculations, and over 7 times speedup to the 16-core parallel job. Moreover, in Fig. 3(b), the t_h curves show algebraic scaling vs. D , i.e., $t_h \sim D^\gamma$, for sufficiently large D where γ values are found slightly less than 4. These appealing benchmarks, together with previous tests in Ref. [42], suggest that GPU acceleration indeed constitutes a very promising technique to be fully explored in quantum manybody computations, particularly in tensor network simulations.

Thermodynamics of finite-size quantum lattice models.— Now we apply ∂ TRG to finite-size chains and cylindrical geometries of finite width W (and length L), and try to approach the thermodynamics limit by increasing the system size. Note that the sweep optimization needs to be adapted when applied to the finite-size systems, i.e., we not only scan $\{w^{(i)}\}$ between different scales but also among different lattice sites/bonds.

For a finite-size system on the 1D or 2D lattice, the high- T

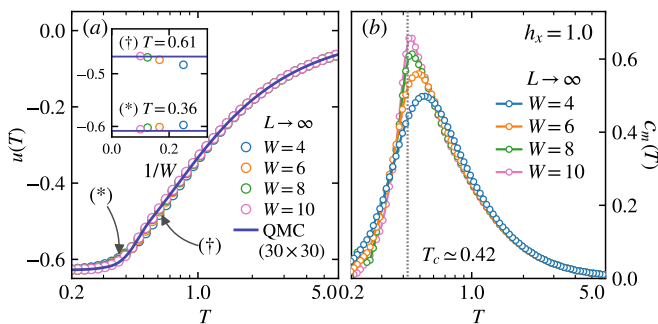


FIG. 5. (Color online) (a) Energy expectation values $u(T)$ and (b) spin specific heat $c_m(T)$ of transverse-field Ising model on cylinders of various widths W and length L extrapolated to infinity. The energy data show excellent agreements with the quantum Monte Carlo (QMC) result on a 30×30 square lattice [43], and the position of peak in $c_m(T)$ provides an accurate estimate, within 2% relative error, of critical temperature.

density matrix $\rho(\tau)$ can be initialized through a discretization-error-free series expansion technique [44] (see SM. F). It has been shown to be preferable, over Trotter-Suzuki type initializations, in dealing 2D systems defined on, e.g., long cylinders [19, 20]. The benchmark results on the finite-size XY chain can be found in SM. H, where deep optimization into n_d layers gains remarkable improvement in accuracy.

As a demonstrative example for 2D simulations, below we focus on the transverse-field Ising model on a square lattice, i.e.,

$$H = \sum_{\langle i,j \rangle} JS_i^z S_j^z - h \sum_i S_i^x, \quad (3)$$

where $J = -1$ (ferromagnetic) is set as the energy scale. The model undergoes a magnetic order-disorder quantum phase transition at a critical field $h_c \approx 1.52219(1)$ [45]. Through a snake-path mapping into quasi-1D lattice [20], the interaction information of the Hamiltonian Eq. (3) on a width W cylinder can be encoded in a compact MPO of bond dimension $D_H = W + 2$ [4, 19]. Given the MPO representation of H , ∂ TRG machinery works automatically and produces accurate results as benchmarked below.

Firstly, we run ∂ TRG simulations on a 4×4 square lattice at the critical transverse field $h = h_c$, and compare the results to exact diagonalization data. In Fig. 4(a), the relative errors $|\delta f/f|$ are plotted vs. β . One can observe a high accuracy with an optimization depth $n_d = 3$, which continuously improves upon increasing the bond dimension D . Moreover, to further reveal the effects of n_d , in Fig. 4(b) we show $|\delta f/f|$ vs. n_d at low temperature, as compared to XTRG data. Indeed the accuracy improves considerably, by orders of magnitude, as n_d increases. For example, the $D = 64, n_d = 4$ ∂ TRG accuracy even goes parallel with the $D = 128$ XTRG one.

Large-scale simulations and finite-temperature phase

transition.— Next, we conduct ∂ TRG calculations of quantum Ising model on wide cylinders with various widths W (up to 10) and lengths L . The transverse field is fixed at $h_x = 1.0 \approx 2/3h_c$, giving rise to a spin order in low temperature. The long-range order melts at a critical temperature $T_c \approx 0.42$, through a second-order phase transition. In Fig. 5, we retain only moderate bond dimension $D = 64$ in the calculations, and the optimization depth is up to $n_d = 4$ layers. The internal energy $u(T)$ and magnetic specific heat $c_m(T)$ are computed from the first and second numerical derivatives of $f(T)$, respectively. Following the line developed in XTRG [19, 20], we exploit a z -shift technique as well as numerical interpolation to collect dense enough data points and ensure a negligible differential error (c.f. SM. I). Moreover, to eliminate the finite-length effects, we perform an extrapolation to $L = \infty$, via linear fitting or energy subtraction (c.f. SM. J).

Collecting the extrapolated data at each width W , we compare the internal energy $u(T)$ with QMC data in Fig. 5(a). A very good agreement of our cylindrical results with the large-scale QMC data is obtained. The latter is computed on a 30×30 square lattice with periodic boundary condition (i.e., torus) which mimics the thermodynamic limit. Furthermore, as shown in the inset, we zoom in at two selected temperatures and find their relative errors $|\delta u/u| < 10^{-3}$ ($W = 10$ result), with respect to QMC. In Fig. 5(b), by further taking the derivatives of internal energy $u(T)$, we obtain the specific heat curves $c_m(T)$. It is observed that the peak in $c_m(T)$ gets sharper as W increases, signaling the existence of a phase transition, and the peak locations for wide cylinders are in good agreement with $T_c \approx 0.42$ in the thermodynamic limit.

Conclusion and outlook.— Inspired by the essential correspondence between the backpropagation algorithm and SRG of tensor networks, we propose the framework of ∂ TRG. With ∂ TRG, we make much better use of tensor parameters by increasing the optimization depth, instead of merely enlarging parameter space dimension D . As a result, a moderate D can lead to an unprecedented high accuracy in simulating thermodynamics of 2D quantum models. Therefore, ∂ TRG constitutes a promising tool to investigate very challenging many-body problems, which are currently of great research interest. These problems include the higher-dimensional classical statistical models, frustrated antiferromagnets, and fermion Hubbard models, etc.

Acknowledgments.— We are indebted to Jian Cui, Jan von Delft, Yannick Meurice, and Andreas Weichselbaum for helpful discussions. This work was supported by the National Natural Science Foundation of China (Grant Nos. 11774420, 11834014, 11974036, and 11774398), the National R&D Program of China (Grants Nos. 2016YFA0300503, 2017YFA0302900) and German Research Foundation (DFG WE4819/3-1) under Germany’s Excellence Strategy - EXC-2111 - 390814868. Our code implementation in PyTorch is publicly available at [this https URL](#).

[1] T. Liu, W. Li, A. Weichselbaum, J. von Delft, and G. Su, “Simple valence-bond crystal in the spin-1 kagome heisenberg an-

tiferromagnet,” *Phys. Rev. B* **91**, 060403 (2015).

- [2] H. J. Liao, Z. Y. Xie, J. Chen, Z. Y. Liu, H. D. Xie, R. Z. Huang, B. Normand, and T. Xiang, “Gapless spin-liquid ground state in the $s = 1/2$ kagome antiferromagnet,” *Phys. Rev. Lett.* **118**, 137202 (2017).
- [3] L. Chen, D.-W. Qu, H. Li, B.-B. Chen, S.-S. Gong, J. von Delft, A. Weichselbaum, and W. Li, “Two-temperature scales in the triangular lattice Heisenberg antiferromagnet,” *Phys. Rev. B* **99**, 140404(R) (2019).
- [4] H. Li, Y.-D. Liao, B.-B. Chen, X.-T. Zeng, X.-L. Sheng, Y. Qi, Z. Y. Meng, and W. Li, “The ghost of a vanishing stripe order in the triangular quantum Ising magnet TmMgGaO_4 ,” [arXiv:1907.08173](https://arxiv.org/abs/1907.08173).
- [5] M. Levin and C. P. Nave, “Tensor renormalization group approach to two-dimensional classical lattice models,” *Phys. Rev. Lett.* **99**, 120601 (2007).
- [6] Z.-C. Gu and X.-G. Wen, “Tensor-entanglement-filtering renormalization approach and symmetry-protected topological order,” *Phys. Rev. B* **80**, 155131 (2009).
- [7] Z. Y. Xie, J. Chen, M. P. Qin, J. W. Zhu, L. P. Yang, and T. Xiang, “Coarse-graining renormalization by higher-order singular value decomposition,” *Phys. Rev. B* **86**, 045139 (2012).
- [8] G. Evenbly and G. Vidal, “Tensor network renormalization,” *Phys. Rev. Lett.* **115**, 180405 (2015).
- [9] G. Evenbly and G. Vidal, “Tensor network renormalization yields the multiscale entanglement renormalization ansatz,” *Phys. Rev. Lett.* **115**, 200401 (2015).
- [10] S. Yang, Z.-C. Gu, and X.-G. Wen, “Loop optimization for tensor network renormalization,” *Phys. Rev. Lett.* **118**, 110504 (2017).
- [11] M. Bal, M. Mariën, J. Haegeman, and F. Verstraete, “Renormalization group flows of Hamiltonians using tensor networks,” *Phys. Rev. Lett.* **118**, 250602 (2017).
- [12] H. C. Jiang, Z. Y. Weng, and T. Xiang, “Accurate determination of tensor network state of quantum lattice models in two dimensions,” *Phys. Rev. Lett.* **101**, 090603 (2008).
- [13] W. Li, S.-J. Ran, S.-S. Gong, Y. Zhao, B. Xi, F. Ye, and G. Su, “Linearized tensor renormalization group algorithm for the calculation of thermodynamic properties of quantum lattice models,” *Phys. Rev. Lett.* **106**, 127202 (2011).
- [14] P. Czarnik, L. Cincio, and J. Dziarmaga, “Projected entangled pair states at finite temperature: Imaginary time evolution with ancillas,” *Phys. Rev. B* **86**, 245101 (2012).
- [15] Y.-L. Dong, L. Chen, Y.-J. Liu, and W. Li, “Bilayer linearized tensor renormalization group approach for thermal tensor networks,” *Phys. Rev. B* **95**, 144428 (2017).
- [16] A. Kshetrimayum, M. Rizzi, J. Eisert, and R. Orús, “Tensor network annealing algorithm for two-dimensional thermal states,” *Phys. Rev. Lett.* **122**, 070502 (2019).
- [17] P. Czarnik and J. Dziarmaga, “Variational approach to projected entangled pair states at finite temperature,” *Phys. Rev. B* **92**, 035152 (2015).
- [18] P. Czarnik and P. Corboz, “Finite correlation length scaling with infinite projected entangled pair states at finite temperature,” [arXiv:1904.02476](https://arxiv.org/abs/1904.02476) (2019).
- [19] B.-B. Chen, L. Chen, Z. Chen, W. Li, and A. Weichselbaum, “Exponential thermal tensor network approach for quantum lattice models,” *Phys. Rev. X* **8**, 031082 (2018).
- [20] H. Li, B.-B. Chen, Z. Chen, J. von Delft, A. Weichselbaum, and W. Li, “Thermal tensor renormalization group simulations of square-lattice quantum spin models,” *Phys. Rev. B* **100**, 045110 (2019).
- [21] S. R. White, “Density matrix formulation for quantum renormalization groups,” *Phys. Rev. Lett.* **69**, 2863–2866 (1992).
- [22] Z. Y. Xie, H. C. Jiang, Q. N. Chen, Z. Y. Weng, and T. Xiang, “Second renormalization of tensor-network states,” *Phys. Rev. Lett.* **103**, 160601 (2009).
- [23] H. H. Zhao, Z. Y. Xie, Q. N. Chen, Z. C. Wei, J. W. Cai, and T. Xiang, “Renormalization of tensor-network states,” *Phys. Rev. B* **81**, 174411 (2010).
- [24] H.-H. Zhao, Z.-Y. Xie, T. Xiang, and M. Imada, “Tensor network algorithm by coarse-graining tensor renormalization on finite periodic lattices,” *Phys. Rev. B* **93**, 125115 (2016).
- [25] G. Carleo and M. Troyer, “Solving the quantum many-body problem with artificial neural networks,” *Science* **355**, 602–606 (2017).
- [26] J. Carrasquilla and R. G. Melko, “Machine learning phases of matter,” *Nature Physics* **13**, 431–434 (2017).
- [27] E. P. L. van Nieuwenburg, Y.-H. Liu, and S. D. Huber, “Learning phase transitions by confusion,” *Nature Physics* **13**, 435–439 (2017).
- [28] E. Stoudenmire and D. J. Schwab, “Supervised learning with tensor networks,” in *Advances in Neural Information Processing Systems 29*, edited by D. D. Lee, M. Sugiyama, U. V. Luxburg, I. Guyon, and R. Garnett (Curran Associates, Inc., 2016) pp. 4799–4807.
- [29] S. Foreman, J. Giedt, Y. Meurice, and J. Unmuth-Yockey, “Examples of renormalization group transformations for image sets,” *Phys. Rev. E* **98**, 052129 (2018).
- [30] Z.-Y. Han, J. Wang, H. Fan, L. Wang, and P. Zhang, “Unsupervised generative modeling using matrix product states,” *Phys. Rev. X* **8**, 031012 (2018).
- [31] C. Guo, Z. M. Jie, W. Lu, and D. Poletti, “Matrix product operators for sequence-to-sequence learning,” *Phys. Rev. E* **98**, 042114 (2018).
- [32] S.-H. Li and L. Wang, “Neural network renormalization group,” *Phys. Rev. Lett.* **121**, 260601 (2018).
- [33] M. Koch-Janusz and Z. Ringel, “Mutual information, neural networks and the renormalization group,” *Nature Physics* **14**, 578–582 (2018).
- [34] H.-J. Liao, J.-G. Liu, L. Wang, and T. Xiang, “Differentiable programming tensor networks,” *Phys. Rev. X* **9**, 031041 (2019).
- [35] A. Paszke, G. Chanan, Z. Lin, S. Gross, E. Yang, L. Antiga, and Z. Devito, “Automatic differentiation in PyTorch,” in *Conference on Neural Information Processing Systems (NIPS 2017)* (Long beach, CA, USA).
- [36] D. E. Rumelhart, G. E. Hinton, and R. J. Williams, “Learning representations by back-propagating errors,” *Nature (London)* **323**, 533–536 (1986).
- [37] D. B. Parker, “Learning logic report,” (1985), [MIT, TR-47](https://arxiv.org/abs/1904.02476).
- [38] Y. LeCun, L. D. Jackel, B. Boser, J. S. Denker, H. P. Graf, I. Guyon, D. Henderson, R. E. Howard, and W. Hubbard, “Handwritten digit recognition: applications of neural network chips and automatic learning,” *IEEE Communications Magazine* **27**, 41–46 (1989).
- [39] *Numerical Optimization*, 2nd ed., Springer Series in Operations Research and Financial Engineering (New York).
- [40] G. Vidal, “Entanglement renormalization,” *Phys. Rev. Lett.* **99**, 220405 (2007).
- [41] G. Evenbly and G. Vidal, “Algorithms for entanglement renormalization,” *Phys. Rev. B* **79**, 144108 (2009).
- [42] A. Milsted, M. Ganahl, S. Leichenauer, J. Hidary, and G. Vidal, “TensorNetwork on TensorFlow: A Spin Chain Application Using Tree Tensor Networks,” (2019), [arXiv:1905.01331](https://arxiv.org/abs/1905.01331).
- [43] B. Bauer et al., “The ALPS project release 2.0: open source software for strongly correlated systems,” *Journal of Statistical Mechanics: Theory and Experiment* **2011**, P05001 (2011).
- [44] B.-B. Chen, Y.-J. Liu, Z. Chen, and W. Li, “Series-expansion thermal tensor network approach for quantum lattice models,”

- [Phys. Rev. B](#) **95**, 161104 (2017).
- [45] H. W. J. Blöte and Y. Deng, “Cluster Monte Carlo simulation of the transverse ising model,” [Phys. Rev. E](#) **66**, 066110 (2002).
- [46] E. Efrati, Z. Wang, A. Kolan, and L. P. Kadanoff, “Real-space renormalization in statistical mechanics,” [Rev. Mod. Phys.](#) **86**, 647–667 (2014).
- [47] K. G. Wilson, “The renormalization group: Critical phenomena and the kondo problem,” [Rev. Mod. Phys.](#) **47**, 773–840 (1975).
- [48] L. P. Kadanoff, “Variational principles and approximate renormalization group calculations,” [Phys. Rev. Lett.](#) **34**, 1005–1008 (1975).
- [49] Y. Lecun, Y. Bengio, and G. Hinton, “Deep learning,” [Nature \(London\)](#) **521**, 436–444 (2015) .
- [50] Here for saving cost, we employ MERA to update the $U^{(i)}$ at the first scale after the environment is obtained, while the rest $U^{(i)}$ on higher layers are update via HOTRG technique.
- [51] See, e.g., <https://github.com/HIPS/autograd>
- [52] The official website of PyTorch can is available at <https://pytorch.org/>

Supplemental Materials: Automatic Differentiation for Second Renormalization Group

Section A. Tensor network representation of the Ising model and its renormalization

In this section, we briefly discuss some basic notions on the real-space tensor renormalization group (TRG) methods, which was referred to as *rewiring method* in literatures, e.g., Ref. [46]. For the sake of simplicity, we take the Ising model on the square lattice as an example. Due to the locality of the interaction, the partition function has a compact tensor-network representation [23], i.e.,

$$Z = \sum_{\{\sigma\}} e^{-\beta H(\{\sigma\})} = \sum_{\{\sigma\}} \prod_a T_{\sigma_i \sigma_j \sigma_k \sigma_l}^{(a)} \quad (\text{A1})$$

where $\{\sigma\}$ denotes the classical spin configurations in the Hamiltonian H . The tensor $T^{(a)}$ is defined on a local plaquette, labeled as a , containing the four original spins. The central idea of renormalization group lies in the concept of renormalization transformation [47, 48], in which a set of new coupling constants $\{K\}$ is sought to represent the Hamiltonian as

$$H = \sum_{a,i} K_i s_i^{(a)}, \quad (\text{A2})$$

where $s_i^{(a)}$ defined at a larger scale is a ‘‘block spin’’, i.e., combination of original spins $\{\sigma\}$ in the plaquette a .

Accordingly, in the rewiring method, TRG finds a set of tensors $\{T^{(a')}\}$ defined at plaquette a' (thus at a larger length scale) to represent the partition function, i.e.,

$$Z = \sum_{\{\alpha\}} \prod_{a'} T_{\alpha_i \alpha_j \alpha_k \alpha_l}^{(a')},$$

where the tensors T are obtained following a similar line of Kadanoff’s RG transformation: We introduce new statistical variables $\{\alpha\}$ (as geometric indices of tensors) and then trace out the original variables $\{\sigma\}$. TRG methods provide accurate tool and versatile platform for studying the conformal criticality and universality near phase transition temperatures [46].

In TRG, the transformations between $T_{\sigma_i \sigma_j \sigma_k \sigma_l}$ at small length scale and $S_{\alpha_i \alpha_j \alpha_k \alpha_l}$ at a larger one constitute the most important parameters of the program. Once the transformations are given, they renormalize the system and result in the partition function Z . In most cases, approximations have to be introduced in the course of TRG, while causing minimal loss in the partition function. We point out that, while most TRG programs employ renormalization transformations that are found only locally [5, 6, 8, 10, 11], the second renormalization group (SRG) [7, 22–24] manages to find proper transformations that optimize the partition function globally.

Section B. Second renormalization group

In the following, we recapitulate SRG in the higher-order tensor renormalization group (HOTRG) algorithm, i.e., HOSRG [7, 24]. For a lattice system with translational invariance, $T^{(i)}$ is used to denote the local tensors renormalized at the i -th scale. $i = 1$ denotes the initial scale at which the original Hamiltonian is defined, and $w^{(i)}$ is the i -th isometric renormalization transformation. The subscripts can be roughly understood as the new statistical variables introduced at different scales, with which the Hamiltonian can be written down, c.f., Eq. (A2). Given the renormalization transformations, we can perform a forward HOTRG iteration,

$$T_{\alpha\beta\gamma\gamma'}^{(i+1)} = \sum_{jx_1x_2x_1'x_2'} T_{x_1x_1'yj}^{(i)} T_{x_2x_2'jy'}^{(i)} w_{x_1x_2\alpha}^{(i)} w_{x_1'x_2'\beta}^{(i)} \quad (\text{B1})$$

as shown in Fig. S1. The transformations $w^{(i)}$ between two scales i and $i + 1$ are determined by the local higher-order singular value decompositions according to tensors $T^{(i)}$.

In the forward HOTRG iteration described above, the transformations $w^{(i)}$ is determined locally [7]. To achieve a global optimization, the environment tensor E should be considered. We punch a ‘‘hole’’ by removing the target tensor in the tensor network and contract all the indices except those of the target. A backward iteration should be involved to accomplish this task and perform the global optimization.

For example, the environment of $T^{(i)}$ at the target scale i can be obtained exploiting the following recursive relation

$$E_{x_1x_1'yj}^{(i,u)} = \sum_{\alpha\beta\gamma'x_2x_2'} E_{\alpha\beta\gamma\gamma'}^{(i+1)} T_{x_2x_2'jy'}^{(i,d)} w_{x_1x_2\alpha}^{(i)} w_{x_1'x_2'\beta}^{(i)} \quad (\text{B2})$$

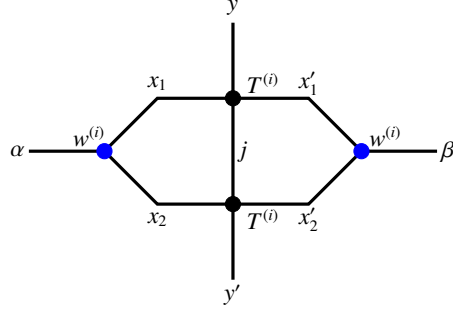


FIG. S1. Illustration of forward process in Eq. (B1). Note that in the backward recursive equation Eq. (B2), the upper $T^{(i)}$ is denoted as $T^{(i;u)}$, and the lower one $T^{(i;d)}$.

where the superscripts $\lambda = (u, d)$ denote the upper and lower $T^{(i)}$ in Fig. S1, and environment $E^{(i)}$ is averaged over two equivalent environment, i.e., $E^{(i)} = \sum_{\lambda} E^{(i;\lambda)}/2$, with $\lambda = u, d$. Given the environment tensor $E^{(i)}$, we can update the renormalization transformation $w^{(i)}$ that globally optimizes the partition function.

Section C. Backpropagation in neural networks

Generally speaking, a deep feedforward neural network sets up a mapping between a set of input signals $x^{(1)}$, such as images, and a set of output signals y , say, categories, through a multi-layer transformation \mathcal{F} , i.e., $y = \mathcal{F}(x^{(1)})$, where \mathcal{F} is represented as a composition of many arranged linear (\mathcal{L}) transformations separated by nonlinear (\mathcal{N}) mappings. To be specific, an n -layer neural network \mathcal{F} can be expressed as

$$\mathcal{F} = \mathcal{N}^{(n)} \mathcal{L}^{(n)} \dots \mathcal{N}^{(2)} \mathcal{L}^{(2)} \mathcal{N}^{(1)} \mathcal{L}^{(1)} \quad (\text{C1})$$

where the linear transformations \mathcal{L} 's contain most of the variational parameters ω 's that need to be optimized. Roughly speaking, the major goal of training a neural network is to find the optimal ω 's which minimize the target objective function L characterizing the discrepancy between the actual and predicted labels.

In essence, each layer of the neural network, i.e., $\mathcal{L}^{(i)}$ followed by $\mathcal{N}^{(i)}$, perform the transformations on the input data/feature $x^{(i)}$, and its output $x^{(i+1)}$ can be regarded as a new representation and a higher-level abstraction of original input [32, 33]. This is very similar to the renormalization transformation of TRG described in the main text, where new bases are introduced in different scales to represent the original partition function.

To train the neural network, the gradients of the objective function L with respect to the parameters ω 's are required for a global optimization. The backpropagation algorithm, arguably the most successful approach for training deep neural networks, exploits the chain rule of derivatives to efficiently compute these gradients [36–38, 49]. To be concrete, the backpropagation method relates the gradients in two neighboring layers as follows

$$\frac{\partial L}{\partial x^{(i)}} = \frac{\partial L}{\partial x^{(i+1)}} \cdot \frac{\partial x^{(i+1)}}{\partial x^{(i)}}. \quad (\text{C2})$$

In deep learning, automatic differentiation (AD) technique is employed to compute the derivative $\frac{\partial L}{\partial x^{(i)}}$ following the recursive equation Eq. (C2), in an analytically rigorous way. Furthermore, the derivatives with respect to the parameters $\omega^{(i-1)}$ can be similarly obtained via one more AD step through $\frac{\partial x^{(i)}}{\partial \omega^{(i-1)}}$, with which one can update $\omega^{(i-1)}$ and regenerate $x^{(i)}$ in the i -th layer.

Section D. Quasi-Newton optimization of isometries

Given the gradient $E_w^{(i)} = \frac{1}{N_1} \overline{w^{(i)}}$ [see Eq. (1) in the main text], the quasi-Newton approach constitutes a class of efficient algorithm for parameter optimization. Here in δ TRG, to impose the isometric constraint, we choose the parametrization $w^{(i)} = \exp(B^{(i)})$, where $B^{(i)}$ is an anti-symmetric real square matrix of dimension D^2 .

With this parameterization, the standard gradient based L-BFGS method [39] can be employed to update $B^{(i)}$ so as to maximize Z . After an exponential operation, we can then compute $\exp(B^{(i)})$ numerically and then truncate this unitary matrix (of dimension D^2 , see main text) into a $D^2 \times D$ isometry $w^{(i)}$.

Note the computational cost of this ‘‘tailored’’ quasi-Newton approach is of time complexity $O(D^6)$, higher than the MERA update $O(D^4)$ that we used in the main text.

Section E. Details on the correspondence between SRG and backpropagation

Suppose the tensor elements in $w^{(i)}$ are independent variational parameters, we can bridge SRG and backpropagation approach, in the context of higher-order tensor renormalizations, by comparing Eq. (B2) and Eq. (C2).

From SRG to backpropagation: Firstly, we assert the following formula which equals ‘‘punching a hole’’ in the tensor network to the derivative

$$E_{abcd}^{(i;\lambda)} = \frac{1}{N_i} \cdot \frac{\partial Z}{\partial T_{abcd}^{(i;\lambda)}} = \frac{\sum_j E_{abcd}^{(i,j;\lambda)}}{N_i}, \quad (\text{E1})$$

where $2N_i = 2^{(n-i+1)}$ is the number of $T^{(i)}$ copies (labeled by index j) in the partition function tensor network, i.e., $Z = \text{Tr}(T^{(i)})^{\otimes 2N_i}$. Matter of fact, the equation

$$Z = \sum_{abcd} T_{abcd}^{(i,j;\lambda)} E_{abcd}^{(i,j;\lambda)}$$

holds at all scales i and location j . Next, we point out that the tensor contractions in Eq. (B2) is nothing but multiplying Jacobian to the tensor $E^{(i+1)}$, i.e.,

$$\frac{\partial T_{a\beta y y'}^{(i+1)}}{\partial T_{x_1 x_1' z j}^{(i;u)}} = \delta_{yz} \cdot \sum_{x_2 x_2'} T_{x_2 x_2' j y'}^{(i;d)} w_{x_1 x_2 \alpha}^{(i)} w_{x_1' x_2' \beta}^{(i)}, \quad (\text{E2})$$

which is the derivative of $T^{(i+1)}$ with respect to $T^{(i;u/d)}$, self-evident in Fig. S1. Combining Eq. (E1) and Eq. (E2) together, we can rewritten Eq. (B2) as

$$\frac{\partial Z}{\partial T_{abcd}^{(i)}} = \sum_{xyzw} \frac{\partial Z}{\partial T_{xyzw}^{(i+1)}} \cdot \frac{\partial T_{xyzw}^{(i+1)}}{\partial T_{abcd}^{(i)}} \quad (\text{E3})$$

where $\frac{\partial T^{(i+1)}}{\partial T^{(i)}} = \sum_{\lambda} \frac{\partial T^{(i+1)}}{\partial T^{(i;\lambda)}}$ is assumed.

Therefore, we reach the conclusion that the recursive relation of environment in the SRG backward iteration, as expressed in Eq. (B2), is exactly the derivative chain rule Eq. (C2) in backpropagation method of deep learning. In Eq. (E3), we have customized the backpropagation with tensor network context to emphasize the in-depth link between the two.

Moreover, to show the correspondence in a more intuitive way, we introduce the following notations

$$\begin{aligned} \begin{array}{c} \textcircled{a} \quad | \quad \textcircled{c} \\ \textcircled{b} \quad | \quad \textcircled{d} \end{array} &\doteq E_{abcd}^{(i)} = \frac{1}{2N_i} \cdot \frac{\partial Z}{\partial T_{abcd}^{(i)}}, \\ \begin{array}{c} \textcircled{x} \quad | \quad \textcircled{z} \quad \textcircled{y} \\ \textcircled{w} \quad | \quad \textcircled{w} \end{array} &\doteq E_{xyzw}^{(i+1)} = \frac{1}{N_i} \cdot \frac{\partial Z}{\partial T_{xyzw}^{(i+1)}}, \end{aligned} \quad (\text{E4})$$

and represent the Jacobian $\frac{\partial T^{(i+1)}}{\partial T^{(i)}}$ in Eq. (E2) as

$$\begin{array}{c} z = c \\ \textcircled{x} \quad \textcircled{a} \quad | \quad \textcircled{b} \quad \textcircled{y} \\ \textcircled{w} \quad \textcircled{d} \end{array} + \begin{array}{c} z \\ \textcircled{x} \quad \textcircled{a} \quad | \quad \textcircled{c} \quad \textcircled{b} \quad \textcircled{y} \\ \textcircled{w} = d \end{array} \doteq \frac{\partial T_{xyzw}^{(i+1)}}{\partial T_{abcd}^{(i)}}. \quad (\text{E5})$$

Then we can picturize Eq. (E3) as

$$\begin{aligned}
 \text{Diagram} &= \frac{1}{2} \times \left[\text{Diagram 1} + \text{Diagram 2} \right] \\
 &= \frac{1}{2} \times \text{Diagram 3} \times \left[\text{Diagram 4} + \text{Diagram 5} \right]
 \end{aligned}
 \tag{E6}$$

where the open indices represent identities, same as those in Eq. (E4) and Eq. (E5).

From backpropagation to SRG: Now we start from Eq. (E3) and try to recover the SRG operation. Given that the tensor network derivative equals environment tensor $E^{(i)}$ (up to a factor), the key step in backpropagation approach is also the computing of Jacobian $\partial T^{(i+1)}/\partial T^i$. In AD technique, this is implicitly expressed as a sequence of tensor contractions exactly reverse the forward process, as also shown in Eq. (E5) (while from right hand side to left). That is to say, the Jacobian is computed in AD by contracting $T_{x_2 x_2' j y'}^{(i;d)}, w_{x_1 x_2 \alpha}^{(i)}, w_{x_1' x_2' \beta}^{(i)}$ with the derivative $\partial Z/\partial T^{(i+1)} = N_{i+1} E^{(i+1)}$ from the $(i+1)$ -th layer. Therefore, we again arrive at Eq. (E6) and confirm that the recursive relation used in SRG is equivalent to the chain-rule AD procedure in backpropagation.

Section F. Initialization of $\rho(\tau)$

In the simulation of quantum lattice models, we start from high temperature density operator $\rho(\tau)$, with a given manybody Hamiltonian H . There are two ways preparing $\rho(\tau)$ and obtaining its matrix product operator (MPO) representation. For infinite 1D quantum chains, we can employ a Trotter-Suzuki decomposition of $\rho(\tau) = e^{-\tau H}$, while for a finite-size system the series expansion technique offers us a discretization-error-free approach to prepare the MPO $\rho(\tau)$. Given the initial $\rho(\tau)$, we can perform successively the exponential cooling procedure down to the require low temperature.

To perform the Trotter-Suzuki decomposition, we rewrite the Hamiltonian

$$H_{XY} = \sum_i h_{i,i+1} = \sum_i S_i^x S_{i+1}^x + S_i^y S_{i+1}^y, \tag{F1}$$

as

$$H_{XY} = H_o + H_e,$$

where $H_{o(e)} = \sum_{i \in \text{odd(even)}} h_{i,i+1}$ contains odd(even) terms. Therefore, up to $O(\tau^3)$ Trotter error, $e^{-\tau H_{XY}} = e^{-\frac{\tau}{2} H_o} e^{-\tau H_e} e^{-\frac{\tau}{2} H_o}$. With sufficiently small τ , e.g., $\tau \simeq 5 \times 10^{-5}$ in Fig. 3, the Trotter error has been very well controlled in practice.

On the other hand, for finite-size systems, including 2D systems mapped into quasi-1D chains with “long-range” interactions, we employ the series expansion of the density matrix

$$e^{-\tau H} = \sum_{n=1}^{N_c} \frac{(-\tau)^n}{n!} H^n, \tag{F2}$$

to realize an initialization of $\rho(\tau)$. By retaining sufficient large N_c , Eq. (F2) is free of any essential expansion error. Therefore, given an MPO representation of H , the density matrix $\rho(\tau)$ can be computed via the series-expansion machinery [44], for both 1D and 2D finite-size systems.

Given the MPO representation of initial $\rho_0(\tau)$ at high temperature, the system can be cooled down linearly (LTRG) [13] or exponentially (XTRG) [17, 19] along the β axis. Thanks to the much less number of truncation steps, it has been shown that XTRG constitutes a more accurate way of thermodynamic simulations [3, 19, 20] and is thus adopted in the current work of ∂ TRG.

Section G. XY chain: computational hours t_h versus β

Here we provide the elapsed real time t_h vs. β in simulating the infinite XY chain. In Fig. S2, we show the $D = 256$ runs with various numbers of CPU cores (Xeon Gold 6230) as well as on the GPU (Tesla V100). We can see clearly a logarithmic scaling between t_h and β , for $\beta \gtrsim 0.1$. This logarithmic instead of linear scaling of wall time t_h vs. β clearly indicates the exponential speed up in ∂ TRG. In addition, from Fig. S2 we can see that in all cases (either GPU or CPU computations with various cores) $\beta = 12.8$, the temperature point we have selected in Fig. 3(b) of the main text, is located well in the logarithmic regime. That is to say, it constitutes a well suitable sampling temperature point for showing t_h vs. D scalings.

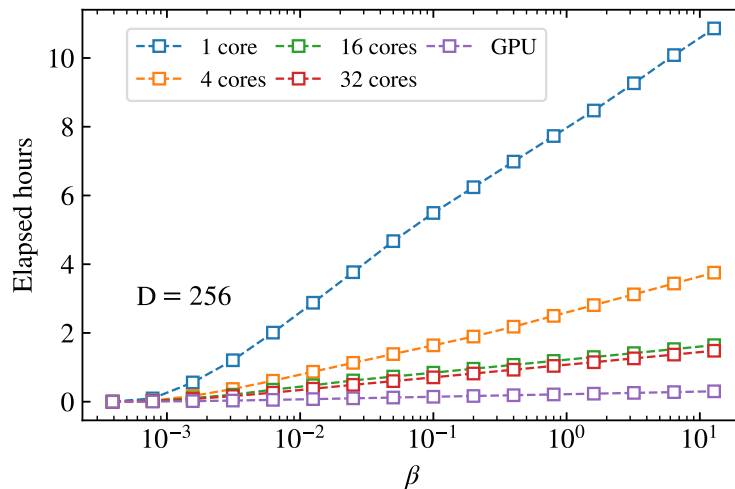


FIG. S2. (Color online) Elapsed hours t_h scaling versus β , where a logarithmic scaling, i.e., $t_h \sim \ln \beta$ can be seen in both GPU and CPU (1, 4, and 16 cores) runs.

Section H. ∂ TRG calculations of finite-size XY chain

Due to the absence of translational invariance in finite-size systems, when applying ∂ TRG to such systems, the isometries w are bond dependent. Therefore, extra care is required in the optimization of w tensors, as will be elaborated below.

Following that introduced in SM. F, we prepare the matrix product operator (MPO) representation of $\rho(\tau)$ via the series expansion. After the initialization, similar to the infinite cases, one perform iteratively renormalization of tensors to cool down the system from high to low temperatures, and can also sweep into inner n_d layers. Nevertheless, there exist in finite-size ∂ TRG algorithms bond-dependent isometries to be optimized, thus sweeps amongst different bonds are required, along with those between different temperature scales.

The finite-size XY spin chain can be solved exactly by a Jordan-Wigner transformation that maps the system into a non-interacting spinless fermion chain, from which the partition function can be readily obtained [19]. In Fig. S3, we perform the calculation of a $L = 50$ XY chain and show the relative errors of free energy for various dimensions D (up to $D = 128$) and depths n_d (up to 3). Similar to the observations for infinite-size chain shown in Fig. 3 of the main text, we can see in Fig. S3 the accuracy improves significantly as the sweep depth n_d increases. Moreover, as shown in Fig. 3, the improvement gets more and more pronounced as D increases from $D = 32$ to 128. In particular, the improvement of accuracies gains over a wide range of temperatures, i.e., from high down to low temperatures. This again reveals unambiguously the advantage of deep optimization in ∂ TRG.

Section I. The z -shift technique

In this appendix, we will briefly recapitulate the z -shift technique for the computation of thermodynamic quantities in ∂ TRG. Below we take the internal energy u as an example, which is obtained by taking numerical derivative of free energy f , i.e.,

$$u \equiv \frac{\partial(\beta f)}{\partial \beta} = \frac{\partial(\beta f)}{\partial \ln \beta} \cdot \frac{1}{\beta} \quad (I1)$$

as adopted in previous XTRG simulations [3, 19, 20]. In the case of the temperature grid denoted as

$$\{\beta_i\} \equiv \{2^i \cdot \tau_0\} = \{\tau_0, 2\tau_0, 4\tau_0, \dots, 2^n \tau_0\}$$

being sparse, one can resort to the z -shift technique by shifting the initial temperature τ by a z -factor

$$\tau = z \cdot \tau_0, \quad \text{with } z \in [0, 2), \quad (I2)$$

and thus obtain a new grid

$$\{z \cdot \beta_i\} \equiv \{2^i \cdot \tau\} = \{\tau, 2\tau, 4\tau, \dots, 2^n \tau\}.$$

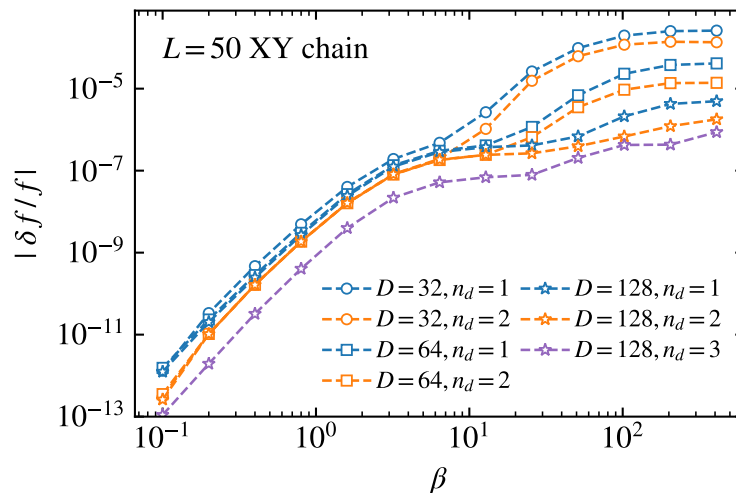


FIG. S3. (Color online) Relative errors of free energy $|\delta f/f|$ in $L = 50$ quantum XY chain computed by ∂ TRG. There is continuous improvement in the accuracies with the increase of bond dimensions $D = 32, 64,$ and $128,$ as well as the sweep depths $n_d = 1, 2,$ and $3.$

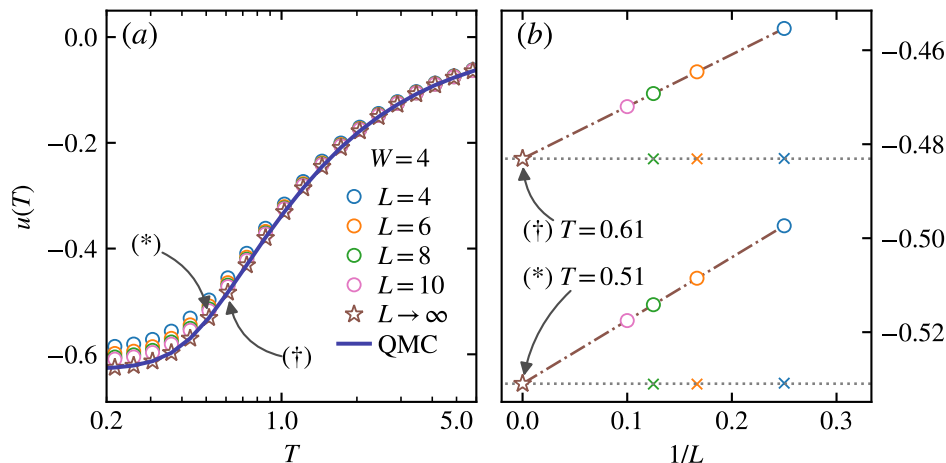


FIG. S4. (Color online) (a) Internal energy $u(T)$ of TFI in field $h_x = 1.0$ with fixed cylinder width $W = 4$ and various L (up to 10), which is used to extrapolate to $L = \infty$. It is benchmarked by QMC data with $W = 4, L = \infty$ with similar extrapolations performed. (b) demonstrates the extrapolations through both the linear fitting and the subtraction technique (depicted as the cross marks), where excellent agreement can be seen between the two schemes. The dotted horizontal line goes strictly through the extrapolated values (the star symbols), which is in perfect agreement with the subtraction results u_{sub} (cross marks).

Note that following the new grid $\{z \cdot \beta_i\}$ the simulations can be performed in parallel to the original $\{\beta_i\}$ run, thus constituting a highly efficient approach in XTRG [19] as well as ∂ TRG.

To be specific, as shown in Fig. 5 of main text, we conduct the ∂ TRG simulations by following 4 sets of temperature grids $\{z \cdot \beta_i\}$ with z -factor chosen to be $z = 2^0, 2^{1/4}, 2^{1/2}, 2^{3/4}$. Before taking the numerical derivative Eq. (11), in practice we further employ an interpolation of free energy data to reach an even denser temperature grid, i.e., totally 16 sets with $z = 2^0, 2^{1/16}, \dots, 2^{15/16}$, which turns out to essentially eliminate the differential errors.

Section J. Energy extrapolations of 2D transverse-field Ising model

In this section, we demonstrate the extrapolations of internal energy $u(T)$ in transverse-field Ising (TFI) model on cylindrical square lattice, via both linear fitting and subtraction methods, as mentioned in the main text. In Fig. S4(a), we show the internal energy in a $W = 4$ TFI model with various length $L = 4, 6, 8, 10$. To some extent, they already show nice convergence with each other as well as to the large-scale QMC data. Nonetheless, one can still extrapolate further to $L = \infty$ limit to eliminate the (small)

finite-size effects, by either linear fitting $u_L = u_\infty + b/L$ or energy subtractions, i.e., $e_{sub} = (e_{L+2} - e_L)/2W$ representing the ‘bulk’ energy. As shown in Fig. S4(b), both schemes generate mutually consistent energies in the $L = \infty$ limit, as indicated by the horizontal grey dotted lines which goes through exactly the extrapolated value [the asterisk symbol in Fig. S4(b)]. Remind that the subtracted energy values get converged much faster to the infinite length limit than linear extrapolation and thus constitutes a more efficient technique in practice for extracting bulk energy expectation values.